Valley-dependent resonant inelastic transmission through a time-modulated region in graphene

T. L. Liu, L. Chang,* and C. S. Chu†

Department of Electrophysics, National Chiao Tung University, Hsinchu 30010, Taiwan, Republic of China

(Received 5 March 2013; revised manuscript received 8 October 2013; published 18 November 2013)

We investigate resonant sideband processes in the transmission through a time-modulated-potential region in graphene. Valley-dependent features in the time-dependent transmission due to trigonal-warping effects in the electronic structures are explored within a tight-binding model. Three main results obtained are dip structures in the transmission, valley dependence of the dip structures, and nontypical-Fabry-Pérot behavior in the dip-structure amplitudes. Dip structures in the transmission are obtained when a relevant band edge is available for the sideband processes. The relevant band edges are shown to become valley dependent, when the incident flow is formed from states of the same group-velocity direction. This is a consequence of the trigonal-warping effects, and it leads to the valley dependence in the dip structures. The dip-structure amplitudes, on the other hand, are found to exhibit a nontypical Fabry-Pérot oscillatory behavior, in their dependence on the width of the time-modulated region. This is shown, in our multiple sideband scattering analysis, to result from resonant sideband processes to a relevant band edge. As such, the nontypical Fabry-Pérot oscillatory behavior serves as another evidence for the key role the relevant band edges play in the transmission dip structures.

DOI: 10.1103/PhysRevB.88.195419 PACS number(s): 72.80.Vp, 73.23.−b, 72.10.Bg

I. INTRODUCTION

The successful fabrication of graphene[1,2] has prompted intensive attention to the utilization of its Dirac fermionlike spectrum and its valley and pseudospin degrees of freedom for novel physical phenomena explorations[3–9] and for carbon-based nanoelectronic applications.[10–17] The two nonequivalent valleys K and K' points (Dirac points) at the corners of the Brillouin zone result from the triangular Bravias lattice, and the amplitudes of the states in the sublattice constitute a pseudospin. Various anomalous phenomena ranging from the Klein tunneling,[18] quantum Hall effects,[19,20] weak (anti-) localization,[21–23] focusing electron flow[24,25] electron beam supercollimation,[26] and edge-states physics[27–32] are attributed to the relativistic dispersion. Exploration of valleytronics in graphene has led to studies on valley filter,[33–37] valley polarization detection,[38] valley physics with broken inversion symmetry,[39] valley physics in strained graphene,[36,40,41] and valley-based qubit in graphene rings[42] and in double quantum dots.[43]

Quantum transport through a time-modulated region in graphene provides us additional knobs for the manipulation of carrier dynamics in the system, through a time-modulated potential,[44–50] or through a time-varying electric field.[51–57] For the case of a time-modulated potential, and focusing upon the low energy regime, when the two-dimensional Dirac equation is at work, phenomena such as photon-assisted transport,[44,45] chiral tunneling,[45] Fano-type resonance,[49] and transverse resonant current[50] are studied. In particular, it was shown that the Klein tunneling, in the total dc transmission and for normal incidence, maintains a perfect transmission by collecting contributions from different sidebands.[45] The Fano-type resonance was demonstrated for non-normal incidence and for the simultaneous presence of a static potential barrier in the time-modulated region.[49] The transverse resonant current could arise, depending on the superposition of the incident states, when the time-modulated region has either linear or oscillatory spatial dependencies.[50] For a short graphene nanoribbon described by a tight-binding model, where levels are all quantized, Fabry-Pérot interference patterns are obtained in the time-modulated-potential-induced conductance.[46] On the other hand, when the time-modulation driving field is an ac and circularly polarized electric field, the pristine graphene is shown to be driven into a topological insulator state.[51–55]

In this paper, we focus upon the valley-dependent nature of the quantum transport through a time-modulated-potential region in graphene. This is an aspect that is relevant to the valleytronics but has not yet been explored in the time-modulated regime. In the dc regime, trigonal warping has recently been invoked for the generation of a fully valley-polarized electron beam in a graphene n-p-n-junction transistor.[34] Here, we study the trigonal-warping effect on the resonant sideband processes, and the manifestations it would allow. Our study is facilitated by a time-dependent wave-function-matching method for the tight-binding model. This allows us to explore the trigonal-warping effects in the vicinity of the low incident energy regime, the regime that is of most interest to valleytronics.

The system we consider in this paper is a two-dimensional graphene sheet with a time-modulated-potential region that has a finite longitudinal width L, along x, and a long transverse extension, along y (see Fig. 1). Transverse open boundaries are not treated in this work. We obtain three main characteristics in the time-dependent transmission: dip structures in the transmission, valley-dependence of these dip structures, and a nontypical-Fabry-Pérot behavior in the dip-structure amplitudes. Dip structures in the transmission occur when the sideband energy $E_n = E_0 + n\hbar\omega$ coincides with a relevant band edge (at energy $E_{\rm B}^*$), where E_0 is the incident energy and ω is the frequency of the time-modulated potential. Conservation of k_y in the transmission causes the relevant band to be a fixed-k_y projection of the graphene energy band. In the vicinity of the Dirac points (located at $\pm K_0\,\hat{x}$), when $\tilde{k}_y \equiv k_y/K_0 \ll 1$, the relevant band picks up an energy gap $\Delta_{\rm g}(\tilde{k}_y)$,

$$\Delta_{\rm g}(\tilde{k}_y) = 2\,\alpha\,t_0|\tilde{k}_y|\left(1-\alpha^2\tilde{k}_y^2/6\right), \tag{1}$$

which increases linearly with $|\tilde{k}_y|$. Here, $\alpha = 2\pi/\sqrt{3}$, and t_0 is the nearest-neighbor hopping coefficient. At the relevant band

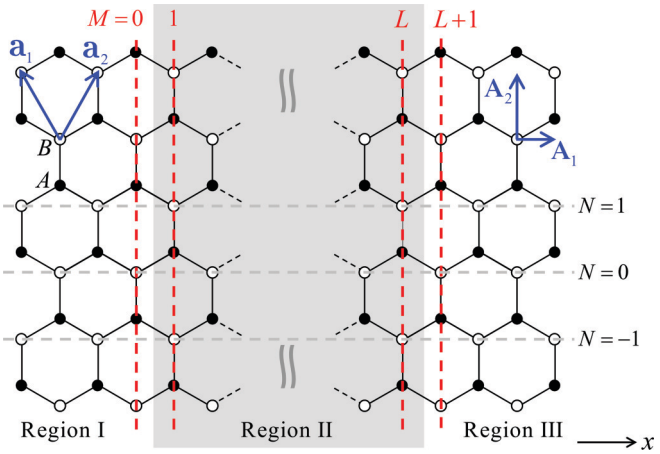

FIG. 1. (Color online) The time-modulated-potential region (gray area) on a graphene sheet is shown extending from $M = 1$ to $M = L$. Indicated are sites A (•) and B (○) in a unit cell, the auxiliary lattice vectors $\{\mathbf{A}_1,\mathbf{A}_2\}$, and the conventional primitive basis vectors $\{\mathbf{a}_1,\mathbf{a}_2\}$.

edge ($E_{\rm B}^* = \pm\Delta_{\rm g}/2$), the longitudinal group velocity $v_{\rm gx}$ is zero, leading to a diverging effective density of states $\mathcal{D}(E \approx E_{\rm B}^*,k_y) = 1/(2\pi\hbar\, v_{gx})$. This provides a favorable condition for the sideband processes and the formation of dip structures in the transmission. Similar sideband processes were found in quasi-one-dimensional electron gas systems that contain a time-modulated potential region.[58,59] In these cases, the relevant bands are naturally given by the subbands in the systems, and the diverging density of states at the subband edges causes the transmission dip structures, due to the sideband processes to the quasi-bound-states formed at the subband edges.[58]

A richer manifestation of the dip structure characteristics is expected in our case, due to the peculiar valley physics in the system. Equation (1) shows, for a given k_y, that the relevant band edge energy $E_{\rm B}^*$ is the same for both valleys (K and K' points). On the other hand, we find out that, for a given group-velocity direction, the k_y values are different near the K and the K' valleys, even though the incident energy E_0 is the same. This is due to the warping effects: For a given group-velocity direction and incident energy E_0, the k_y magnitude is smaller near the K valley and larger near the K' valley. Thus the relevant band edge energy $E_{\rm B}^*$ as well as the transmission dip structures become valley dependent. These valley dependent features in the time-dependent transmission will be of use if incident flow can be formed from states of the same group-velocity direction. Fixing φ, the angle denoting the direction of the incident group velocity, can be achieved by the collimation of incident flow. This has been achieved experimentally, in two-dimensional electron systems, by the alignment of two point contacts in series.[60,61] It should thus be of interest for future exploration on electron beam focusing and collimation in graphene.[24–26] In this work, a finite valley polarization $\mathcal{P}$ is obtained in the transmitted beam even when the collimation angle φ has a finite angle range $\Delta\varphi$. Finally, the nontypical-Fabry-Pérot behavior in the dip-structure amplitudes is found, according to our detail multiple sideband scattering analysis, to originate from interference between multiple inelastic sideband processes to the relevant band edge.

This paper is organized as follows. In Sec. II, we present our time-dependent wave-function matching method. We also present an alternate approach, namely the multiple sideband scattering approach, which is utilized for the analysis of the physical mechanism behind the nontypical-Fabry-Pérot behavior in the dip-structure amplitudes. Numerical results and discussions are presented in Sec. III. Finally, a conclusion is presented in Sec. IV.

II. THEORY

In this section, we present the theory for time-dependent transmission in a graphene sheet. The graphene sheet is assumed to be of infinite extent, with no open boundary, and the time-modulated-potential (gray area in Fig. 1) region has its boundaries running along an armchair chain. The conventions and notations that we adopt in this work are described below along with the introduction of our basic model. The unit cells in Fig. 1 are denoted by $\mathbf{R}_j = M_j\mathbf{A}_1 + N_j\mathbf{A}_2$, where the auxiliary lattice vectors $\mathbf{A}_1 = \sqrt{3}a_0/2\,\hat{x}$ and $\mathbf{A}_2 = 3a_0/2\,\hat{y}$ are chosen such that $M_j \pm N_j$ must be even integers. Here $a_0 = 1.42$ Å is the distance between neighboring carbon atoms. The Dirac points are located at $\pm K_0\hat{x}$, where $K_0 = 2\pi/3A_1$. A more conventional choice for the Bravais lattice vectors is denoted by $\mathbf{a}_1$ and $\mathbf{a}_2$ in Fig. 1.

The time-dependent Hamiltonian is given by $H = H_0 + V(t)$, where

$$H_0 = -t_0\sum_{\langle i,j\rangle}(\hat{a}_i^\dagger\hat{b}_j + \hat{b}_j^\dagger\hat{a}_i) + \Delta\sum_i(\hat{a}_i^\dagger\hat{a}_i - \hat{b}_i^\dagger\hat{b}_i), \tag{2}$$

and

$$V(t) = \sum_i V(M_i,t)\,(\hat{a}_i^\dagger\hat{a}_i + \hat{b}_i^\dagger\hat{b}_i). \tag{3}$$

Here Δ is included in H_0 to facilitate our study of the time-dependent transport characteristics of nongapped (pristine, with $\Delta = 0$) and gapped ($\Delta \neq 0$) graphene. $\hat{a}_j^\dagger$ ($\hat{a}_j$) is the creation (annihilation) operator for an electron at the A site of the jth unit cell, and $t_0 = 2.66$ eV is the nearest-neighbor hopping coefficient. The time-modulated potential occurs only in region II, with a form

$$V(M,t) = \begin{cases} V_0\cos(\omega t) & 1 \leqslant M \leqslant L, \\ 0 & \text{otherwise.} \end{cases} \tag{4}$$

A Bloch state $|\Psi_{\mathbf{k}}^{\rm B}\rangle$ incident upon this potential is scattered into the scattering state $|\Psi_{\mathbf{k}}^{\rm (sc)}\rangle$. Here $\mathbf{k} = \mathbf{p}_0^{(\mu)}$ is the incident momentum at energy E_0 and μ is the incident valley index. The index denotes valley K (K') by $\mu = 1$ (2), and right- (left-) going state is denoted by momentum $\mathbf{p}$ ($\mathbf{q}$). As k_y is conserved in the scattering, we can express the scattering state in the form

$$\left|\Psi_{\mathbf{k}}^{\rm (sc)}\right\rangle = \sum_{j,s} e^{ik_yN_jA_2}\, f_{s\,\mathbf{k}}(M_j,t)\,|j,s\rangle, \tag{5}$$

where $s = A(B)$ is the site index, and A_2 is the magnitude of $\mathbf{A}_2$. Time evolution of $f_{s\,\mathbf{k}}(M,t)$ is obtained by substituting

Eq. (5) into Eq. (2) and Eq. (3) to give

$$\frac{\partial}{\partial t}\mathbf{F}_{\mathbf{k}}(M,t) = -\frac{i}{\hbar}[V(M,t)+\Delta\,\sigma_z]\,\mathbf{F}_{\mathbf{k}}(M,t) + \frac{it_0}{\hbar}[\,\mathbf{T}\,\mathbf{F}_{\mathbf{k}}(M+1,t)+\mathbf{T}\,\mathbf{F}_{\mathbf{k}}(M-1,t)] + \frac{it_0}{\hbar}\,\sigma_x\,\mathbf{F}_{\mathbf{k}}(M,t), \tag{6}$$

where the hopping matrix $\mathbf{T}$ is given by

$$\mathbf{T} = \begin{pmatrix} 0 & e^{-ik_yA_2} \\ e^{ik_yA_2} & 0 \end{pmatrix} \tag{7}$$

and

$$\mathbf{F}_{\mathbf{k}}(M,t) = \begin{pmatrix} f_{A\,\mathbf{k}}(M,t) \\ f_{B\,\mathbf{k}}(M,t) \end{pmatrix}. \tag{8}$$

The form of $V(M,t)$ in Eq. (3) has $\mathbf{F}_{\mathbf{k}}$ divided into three pieces: $\mathbf{F}_{\mathbf{k}}(M,t)=\mathbf{F}^{(\mathrm{I})}_{\mathbf{k}}(M,t)$ when $M\leqslant 0$, $\mathbf{F}_{\mathbf{k}}(M,t)=\mathbf{F}^{(\mathrm{II})}_{\mathbf{k}}(M,t)$ when $1\leqslant M\leqslant L$, and $\mathbf{F}_{\mathbf{k}}(M,t)=\mathbf{F}^{(\mathrm{III})}_{\mathbf{k}}(M,t)$ when $L+1\leqslant M$. Each $\mathbf{F}^{(\mathrm{i})}_{\mathbf{k}}(M,t)$ satisfies their own time-evolution equation, Eq. (6), in their respective M ranges.

These three pieces of $\mathbf{F}_{\mathbf{k}}$ are connected, at all time t, by the conditions

$$\mathbf{F}^{(\mathrm{I})}_{\mathbf{k}}(0,t)=\tilde{\mathbf{F}}^{(\mathrm{II})}_{\mathbf{k}}(0,t),\quad \mathbf{F}^{(\mathrm{II})}_{\mathbf{k}}(1,t)=\tilde{\mathbf{F}}^{(\mathrm{I})}_{\mathbf{k}}(1,t), \tag{9}$$

at the left boundary, and the conditions

$$\begin{aligned}\mathbf{F}^{(\mathrm{II})}_{\mathbf{k}}(L,t)&=\tilde{\mathbf{F}}^{(\mathrm{III})}_{\mathbf{k}}(L,t),\\ \mathbf{F}^{(\mathrm{III})}_{\mathbf{k}}(L+1,t)&=\tilde{\mathbf{F}}^{(\mathrm{II})}_{\mathbf{k}}(L+1,t),\end{aligned} \tag{10}$$

at the right boundary, where $\tilde{\mathbf{F}}^{(i)}_{\mathbf{k}}(M,t)$ is the auxiliary function obtained from *analytic continuing* of the function $\mathbf{F}^{(i)}_{\mathbf{k}}(M,t)$ to a location M outside its own M range.

The number current density along $\hat{x}$ at location M due to $|\Psi^{(\mathrm{sc})}_{\mathbf{k}}\rangle$ is given by

$$\begin{aligned} j^{(\mathrm{sc})}_{\mathbf{k}\,x}(M,t) &= \langle\Psi^{(\mathrm{sc})}_{\mathbf{k}}|\,\hat{j}_x(M)\,|\Psi^{(\mathrm{sc})}_{\mathbf{k}}\rangle \\ &= \frac{it_0}{2\hbar}[(\mathbf{F}^{\dagger}_{\mathbf{k}}(M+1,t)-\mathbf{F}^{\dagger}_{\mathbf{k}}(M-1,t))\mathbf{T}\mathbf{F}_{\mathbf{k}}(M,t)-\mathrm{c.c.}]. \end{aligned} \tag{11}$$

Equation (11) is used for the calculation of the transmission current and for the checking of the current conservation of our time-dependent transmission results. In particular, the dc component of $j^{(\mathrm{sc})}_{\mathbf{k}\,x}$ should remain position (or M) independent in the presence of evanescent modes.

Expressing explicitly in terms of the reflection coefficients $\mathcal{R}^{(\nu)}_m$ and transmission coefficients $\mathcal{T}^{(\nu)}_m$, the $\mathbf{F}_{\mathbf{k}}(M,t)$ functions in their respective M ranges are of the form

$$\begin{aligned} \mathbf{F}^{(\mathrm{I})}_{\mathbf{k}}(M,t) &= \sum_{m,\nu}\left(\mathbf{F}^{(\mathrm{B})}_{\mathbf{k}}(M)\,\delta_{m0}\,\delta_{\mu\nu}+\mathcal{R}^{(\nu)}_m\,\mathbf{F}^{(\mathrm{B})}_{\mathbf{q}^{(\nu)}_m}(M)\right)e^{-iE_mt/\hbar}, \\ \mathbf{F}^{(\mathrm{II})}_{\mathbf{k}}(M,t) &= \sum_{m,l,\nu}\left(\mathcal{A}^{(\nu)}_l\,\mathbf{F}^{(\mathrm{B})}_{\mathbf{p}^{(\nu)}_l}(M)+\mathcal{B}^{(\nu)}_l\,\mathbf{F}^{(\mathrm{B})}_{\mathbf{q}^{(\nu)}_l}(M)\right) \\ &\quad\times J_{m-l}(V_0/\hbar\omega)\;e^{-iE_mt/\hbar}, \\ \mathbf{F}^{(\mathrm{III})}_{\mathbf{k}}(M,t) &= \sum_{m,\nu}\mathcal{T}^{(\nu)}_m\,\mathbf{F}^{(\mathrm{B})}_{\mathbf{p}^{(\nu)}_m}(M)\;e^{-iE_mt/\hbar}. \end{aligned} \tag{12}$$

Here $E_m=E_0+m\hbar\omega$ is the energy in the mth sideband, and $J_m(z)$ is the mth order Bessel function of the first kind. $\mathbf{F}^{(\mathrm{B})}_{\mathbf{p}^{(\nu)}_l}(M)$ is a column vector

$$\mathbf{F}^{(\mathrm{B})}_{\mathbf{p}^{(\nu)}_l}(M)=\left(f^{(B)}_{A\,\mathbf{p}^{(\nu)}_l},\,f^{(B)}_{B\,\mathbf{p}^{(\nu)}_l}\right)^T, \tag{13}$$

formed from the site coefficients $f^{(\mathrm{B})}_{s\,\mathbf{p}^{(\nu)}_l}(M)$ of the Bloch state for $\mathbf{p}^{(\nu)}_l=(p^{(\nu)}_{l\,x},k_y)$ and at energy E_l. By making connection with the Bloch state

$$\left|\Psi^{(\mathrm{B})}_{\mathbf{p}}\right\rangle=\sum_{j,s}e^{ik_yN_jA_2}\,f^{(\mathrm{B})}_{s\,\mathbf{p}}(M_j)\,|j,s\rangle\;e^{-iE_lt/\hbar}, \tag{14}$$

we obtain

$$\mathbf{F}^{(\mathrm{B})}_{\mathbf{p}}(M)=\mathcal{N}_{\mathbf{p}}\;e^{ip_xMA_1}(H_{\mathbf{p}},\,E_{\mathbf{p}}-\Delta)^T, \tag{15}$$

with

$$E_{\mathbf{p}}=\pm\sqrt{H_{\mathbf{p}}\tilde{H}_{\mathbf{p}}+\Delta^2} \tag{16}$$

the electron- (hole-)like branch, $H_{\mathbf{p}}=-t_0[1+2e^{-ik_yA_2}\cos(p_xA_1)]$, $\tilde{H}_{\mathbf{p}}=-t_0[1+2e^{ik_yA_2}\cos(p_xA_1)]$, and $\mathcal{N}_{\mathbf{p}}$ is the normalization constant. Note that $\tilde{H}_{\mathbf{p}}\neq H^*_{\mathbf{p}}$ for evanescent waves, and the column vector in Eq. (15) is reckoned as a pseudospin state.

The current transmission $T^{(\mu)}(E_0)$ is obtained by solving the coefficients $\mathcal{R}^{(\nu)}_m$,$\mathcal{A}^{(\nu)}_m$,$\mathcal{B}^{(\nu)}_m$, and $\mathcal{T}^{(\nu)}_m$ directly from Eq. (12) while imposing the boundary conditions in Eq. (9) and Eq. (10). In terms of the coefficients $\mathcal{T}^{(\nu)}_m$, the dc current transmission is given by[45]

$$T^{(\mu)}(E_0)=\frac{j^{(sc)}_{\mathbf{k},x}}{j^{(\mathrm{B})}_{\mathbf{k},x}}=\sum_{m,\nu}\left|\mathcal{T}^{(\nu)}_m\right|^2\frac{j^{(\mathrm{B})}_{\mathbf{p}^{(\nu)}_m,x}}{j^{(\mathrm{B})}_{\mathbf{p}^{(\mu)}_0,x}}\;, \tag{17}$$

where $j^{(\mathrm{B})}_{\mathbf{k},x}$ is essentially the time average of the current in Eq. (11) albeit replacing the scattering state by the corresponding Bloch state. The dependencies of $T^{(\mu)}(E_0)$, or for that matter T_m, where $T^{(\mu)}(E_0)=\sum_m T_m$, on E_0, μ, and L have shown important resonant sideband characteristics. These characteristics and the underlying mechanisms are the main focuses of our study in this paper. Whenever there is no ambiguity, we will suppress the μ superscript, keeping only the sideband index m in T_m.

We have also solved the current transmission $T^{(\mu)}(E_0)$ by another approach, namely the multiple sideband scattering approach. This latter approach provides us a more transparent extraction of physical mechanisms behind various transmission characteristics. Essentially, the scattering matrices $\mathbf{S}^{(\mu)}_1$ and $\mathbf{S}^{(\mu)}_2$ for the scattering at the left and the right boundaries

of the time-modulated potential region are determined by applying Eq. (6) to the respective boundary. These matrices are of the form

$$\mathbf{S}_i^{(\mu)}(E_0) = \begin{pmatrix} \mathbf{t}_i' & \mathbf{r}_i \\ \mathbf{r}_i' & \mathbf{t}_i \end{pmatrix}, \tag{18}$$

where the *primed* (non-*primed*) submatrices take on right- (left-) going incident channels, while $\mathbf{r}_i$ ($\mathbf{t}_i$) submatrices denote *reflection* (*transmission*) processes. Again, the superscript μ are suppressed in the submatrices. The channels in each submatrix include both sideband and valley indices. The coefficients $\mathcal{R}_m^{(\nu)}, \mathcal{A}_m^{(\nu)}, \mathcal{B}_m^{(\nu)}, \mathcal{T}_m^{(\nu)}$ are then expressed in terms of the above submatrices, given by

$$\mathcal{R}_m^{(\nu)} = \langle q_m^{(\nu)} | \mathbf{r}_1' + \mathbf{t}_1 \mathbf{r}_2' \frac{\mathbf{1}}{\mathbf{1} - \mathbf{r}_1 \mathbf{r}_2'} \mathbf{t}_1' | p_0^{(\mu)} \rangle, \tag{19a}$$

$$\mathcal{A}_m^{(\nu)} = \langle p_m^{(\nu)} | \frac{\mathbf{1}}{\mathbf{1} - \mathbf{r}_1 \mathbf{r}_2'} \mathbf{t}_1' | p_0^{(\mu)} \rangle, \tag{19b}$$

$$\mathcal{B}_m^{(\nu)} = \langle q_m^{(\nu)} | \mathbf{r}_2' \frac{\mathbf{1}}{\mathbf{1} - \mathbf{r}_1 \mathbf{r}_2'} \mathbf{t}_1' | p_0^{(\mu)} \rangle, \tag{19c}$$

$$\mathcal{T}_m^{(\nu)} = \langle p_m^{(\nu)} | \mathbf{t}_2' \frac{\mathbf{1}}{\mathbf{1} - \mathbf{r}_1 \mathbf{r}_2'} \mathbf{t}_1' | p_0^{(\mu)} \rangle, \tag{19d}$$

where the bra (ket) is to pick up the desired incident (transmitted) channels in the column (row) of the submatrices. Both this multiple sideband scattering approach and the aforementioned direct-matching approach give the same results in our numerical calculations.

III. RESULTS AND DISCUSSIONS

In this section, we present numerical results for the current transmission characteristics through a time-modulated-potential region in pristine graphene. Results for gapped graphene will be included for comparison purposes. Demonstrated in the following subsections are the transmission dip structures, the valley dependence of these dip structures, and the nontypical Fabry-Pérot resonance nature of the dip-structure amplitudes.

A. Transmission dip structures and their valley dependence

The dip structures in the current transmission are presented in Fig. 2, when $T^{(\mu)}$ versus E_0 is shown for fixed k_y values. This figure provides a straightforward exposition of the physical origin for the dip structures. In Fig. 2, the time-modulated potential acting upon a pristine graphene has a longitudinal length LA_1 ($L = 150$), frequency $\hbar\omega = 0.1\,t_0$, and potential amplitude $V_0 = 0.05\,t_0$. The lower figure of Fig. 2 shows that the dip structures occur in all the transmission curves, including states incident from either valley K or K', and for k_y fixed at values k_{y1} or k_{y2}. More importantly, the E_0 locations of the dip structures are identified, according to the relevant bands shown in Fig. 2 (upper figure), to be at $E_0 = E_B^*(k_y) + \hbar\omega$. Here $E_B^*(k_y)$ is the relevant band-edge energy associated with the relevant band gap, given by Eq. (1). E_B^* is also the threshold energy for $T^{(\mu)}(E_0)$, below which the transmission drops abruptly to zero. For $k_{y1} = 0.029\,K_0$ and $k_{y2} = 0.044\,K_0$, Fig. 2 shows that $E_B^*(k_y)$ increases with k_y in the $k_y \ll K_0$ regime, a result that is contained in Eq. (1). These transmission

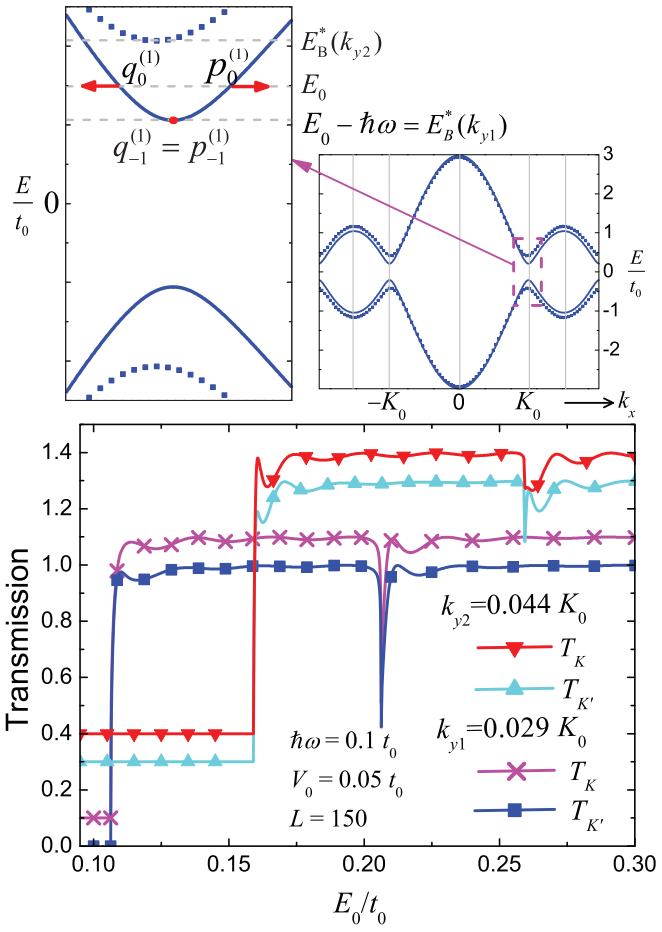

FIG. 2. (Color online) Relevant bands and current transmission $T^{(\mu)}(E_0)$ for fixed k_y. In the upper figure, the relevant band for $k_{y1} = 0.029\,K_0$ ($k_{y2} = 0.044\,K_0$) is denoted by the solid (dashed) curve. Blowups of the relevant bands show K-valley band edges $E_B^*(k_{y1})$ and $E_B^*(k_{y2})$ for the corresponding k_y values, and the momenta for the $n = 0$ and the $n = -1$ sidebands for $k_y = k_{y1}$. Transmission curves (lower figure) for incident states from valley K ($\mu = 1$) are denoted by $\times$ (k_{y1}) and $\blacktriangledown$ (k_{y2}), and that from valley K' ($\mu = 2$) are denoted by $\blacksquare$ (k_{y1}) and $\blacktriangle$ (k_{y2}). The time-modulated potential has a longitudinal length LA_1 ($L = 150$), $\hbar\omega = 0.1\,t_0$, and $V_0 = 0.05\,t_0$. Dip structures in $T^{(\mu)}(E_0)$ occur at $E_B^* + \hbar\omega$.

dip-structure characteristics are understood as the resonant sideband processes the transmitting electrons undergo to the relevant band edge, whenever $E_B^* = E_0 - n\hbar\omega = E_{-n}$, at which the effective density of states is singular. The effective density of states $\mathcal{D}(E = E_{\mathbf{k}}, k_y) = 1/(2\pi\hbar\, v_{gx})$, with the longitudinal group velocity v_{gx}, given by

$$v_{gx} = \frac{2t_0 A_1}{\hbar} \left| \frac{\sin(k_x A_1)[\cos(k_y A_2) + 2\cos(k_x A_1)]}{E_{\mathbf{k}}} \right|, \tag{20}$$

vanishes at $E = E_B^*$.

A closer look at the E_0 dependence of the sideband coefficients in Eq. (12) finds (not shown here) a simultaneous occurrence of the $T^{(\mu)}$ dip structures and the peaking of the coefficients $|\mathcal{A}_{-1}^{(\nu)}|$ and $|\mathcal{B}_{-1}^{(\nu)}|$. This corroborates that the resonant sideband processes are prompted by the singular effective density of states of the relevant band edge, when the sideband E_{-1} aligns with E_B^*.

On the one hand, the dip structures in Fig. 2 do not exhibit valley-dependent characteristics. This is seen by comparing, for the k_{y1} case, the transmission curves for incident valleys $\mu = 1$ and $\mu = 2$, denoted by symbols $\times$ and ■, respectively. The valley-independent feature is related to the fact that $E_B^*(k_y)$ bears the same value at both valleys, as is evident from the relevant bands shown in Fig. 2 (upper figure). On the other hand, the $T^{(\mu)}(E_0)$ for given k_y value is of pedagogical importance in establishing the physical origin of the transmission dip structures. A scheme more relevant to experiment is in order here. In the following, we propose considering $T^{(\mu)}(E_0)$ for incident flow formed from states of the same group-velocity direction. This collimation of electron beam has been achieved experimentally in two-dimensional electron systems, by the alignment of two point contacts in series.[60,61] We explore the $T^{(\mu)}(E_0)$ characteristics for given φ, the angle the incident beam group velocity formed with the $\hat{x}$ direction.

Current transmission characteristics $T^{(\mu)}$-E_0 for fixed φ values are presented in Figs. 3(a) and 3(b), for states incident from K' and K valley, respectively. The time-modulated potential has a longitudinal length $L = 110$, frequency $\hbar\omega = 0.1\,t_0$, and potential amplitude $V_0 = 0.05\,t_0$. All $\varphi \neq 0$ curves exhibit dip structures. The absence of dip structures in the

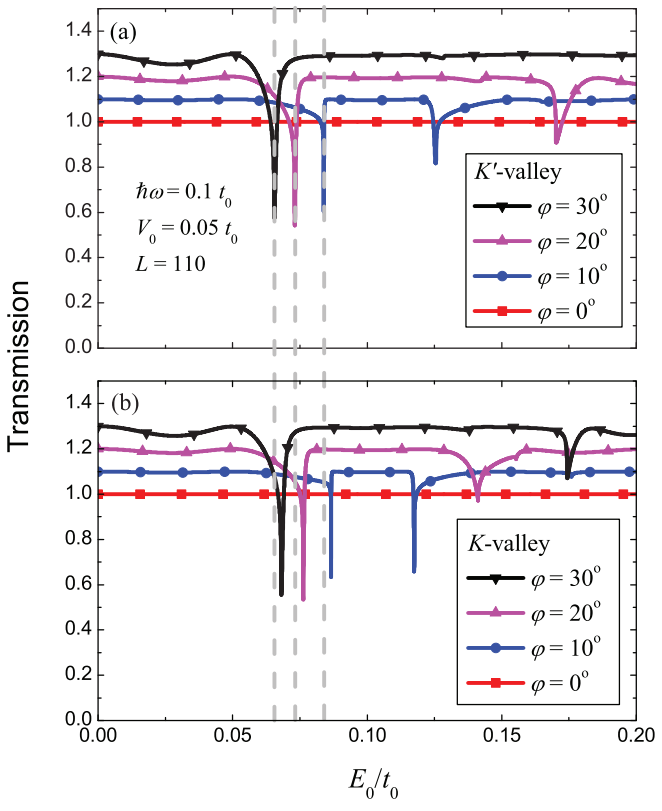

FIG. 3. (Color online) Current transmission $T^{(\mu)}$ versus incident energy E_0 for given group-velocity directions φ. Curves for $\varphi = 0^\circ$, 10°, 20°, and 30° are denoted by symbols square, sphere, triangle, and inverted triangle, respectively. Upper (lower) figure is for incident valley K' (K). Curves are vertically shifted by 0.1 for better presentation. The time-modulated potential has a longitudinal length $L = 110$, $V_0 = 0.05t_0$, and $\hbar\omega = 0.1t_0$. The vertical dashed lines are guides to illustrate the valley dependence in the transmission dip structures.

$\varphi = 0^\circ$ (or $k_y = 0$) curves is consistent with the fact that the relevant band has no energy gap in the low energy regime $E_0 \sim \hbar\omega$. While all the dip structures exhibit valley-dependent features, those that occur in the lower E_0 have weaker valley dependence. As φ increases, the lower (higher) E_0 dip structures shift towards lower (higher) E_0 values. The higher energy dip structure for $\varphi = 30^\circ$ is out of the E_0 range in the figure. A check on the sideband coefficients reveals that all the dip structures shown are associated with $n = -1$ sideband processes. All these can be explained by the resonant sideband processes, with the recognition that here k_y is no longer fixed, but becomes $k_y(\varphi,\mu,E_0)$, where μ is the valley index. A more explicit exposition of $k_y(\varphi,\mu,E_0)$ will be given in the following, but we want to give a simple picture here first.

With $k_y(\varphi,\mu,E_0)$ becoming a function of φ, E_0, and μ, different relevant energy bands will be invoked at different E_0 values for the resonant sideband processes consideration. It is found that $k_y(\varphi,1,E_0) \approx k_y(\varphi,2,E_0)$ for $E_0 \approx 0$, but $k_y(\varphi,1,E_0) < k_y(\varphi,2,E_0)$ for larger E_0 and for $\varphi < \pi/3$. This difference in k_y is due to the warping effect. It leads to a smaller effective energy gap in the relevant band for the K-valley incident beam than for the K'-valley incident beam, and subsequently, leads to the valley dependence in the dip structures. The lower (higher) energy dip structures in Fig. 3 are the $n = -1$ sideband processes to the relevant band edge of the negative (positive) energy relevant band, with the resonant condition $E_0 = \mp E_B^*(k_y) + \hbar\omega$. Roughly speaking, subjected to corrections from warping effect, the ΔE_0 between the two dips structures in the same $T^{(\mu)}$-E_0 curve gives us the energy gap of the relevant band. The general trend of the dip-structure E_0-shifts with φ reflects the increasing of k_y with φ. Finally, comparing with Fig. 2, the missing of the $E_0 = -E_B^*(k_y) + \hbar\omega$ dip structure there is due to the suppression of such process when $\Delta_g < \hbar\omega$ is not satisfied. Moreover, in the $E_0 \approx 0$ region, energy gap approaches zero (as $k_y \approx 0$), so that there is no thresholdlike $T^{(\mu)}$-E_0 behavior in Fig. 3.

For comparison purposes, the case of a gapped graphene is presented in Fig. 4. The $T^{(\mu)}$-E_0 exhibits thresholdlike behavior near $E_0 \approx 0$. Here, except for $\Delta = 0.01\,t_0$, the other physical parameters are the same as in Fig. 3. All the curves shown have the same threshold energy even though φ values are different. This shows that all the constant φ contours converge to the same band edge energy Δ in the $E_0 \approx 0$ region. Specifically, dip structures are found in the $\varphi = 0$ curve, with the energy separation equal to 2Δ. Other dip structures remain essentially the same as in Fig. 3, since $\Delta = 0.01\,t_0$ is quite small.

The trigonal warping effect is explicitly shown in Fig. 5 (lower figure), where contour plots of both φ and E are made in the Brillouin zone. This result is obtained from Eq. (16) and Eq. (20). Special symmetry points in the Brillouin zone (dashed hexagon) are indicated in the upper figure of Fig. 5. The φ contours are depicted by lines fanning out from these special points, whereas the E-contour lines encircle the Γ and K points. We note that a φ-contour line does not necessarily cross the E contours normally. It is because connecting points of the same group-velocity direction in the Brillouin zone does not require the group-velocity direction to lie along the φ contour. The trigonal-warping effect causes the E contour around the K point to evolve from a circularlike shape into a concave-triangularlike shape, as E increases. More

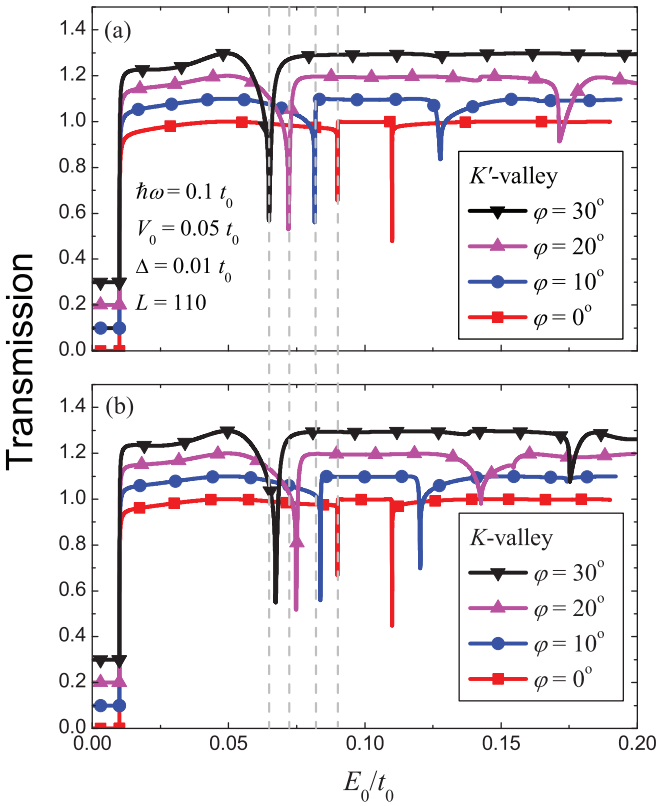

FIG. 4. (Color online) Current transmission $T^{(\mu)}$ versus incident energy E_0 for a gapped ($\Delta = 0.01t_0$) graphene and for given group-velocity directions φ. Curves for $\varphi = 0^\circ$, 10°, 20°, and 30° are denoted by symbols square, sphere, triangle, and inverted triangle, respectively. Upper (lower) figure is for incident valley K' (K). Curves are vertically shifted by 0.1 for better presentation. The time-modulated potential has a longitudinal length $L = 110$, $V_0 = 0.05t_0$, and $\hbar\omega = 0.1t_0$. The vertical dashed lines are guides to illustrate the valley-dependence in the transmission dip structures.

importantly, the orientation of the triangularlike E contour encircling the K point is different from that encircling the K' point. As a result, φ contours emanating from the K point, for $\varphi < \pi/3$, will converge onto the M point, as E_0 increases from zero to t_0. But the φ contours that emanate from the K' point, for $0 < \varphi < 2\pi/3$, will converge onto the M' point. This provides a pictorial insight to the result $k_y(\varphi,1,E_0) < k_y(\varphi,2,E_0)$ for $\varphi < \pi/3$, and for $0 < E_0 < t_0$. The insight is the key for the understanding of the valley dependence in the sideband processes, and hence to the valley-dependent resonant transmission.

Analytical expressions for the position of the dip structures, as shown in Fig. 3 (for the $\Delta = 0$ cases), can be obtained. With $\mathbf{q} = (\mathbf{k} - \mu K_0\hat{x})/K_0$, and expanding up to the fourth order in $\mathbf{q}$ in the dispersion relation of graphene, we obtain q_x as a function of q_y and at energy $E = \pm E_B^*(q_y) + \omega$, given by

$$q_x \simeq \frac{\omega}{\alpha}\sqrt{1 \pm \frac{2\alpha q_y}{\omega}} + \frac{\mu\omega^2}{6\alpha}\left[1 \pm \frac{2\alpha q_y}{\omega} - 3\left(\frac{\alpha q_y}{\omega}\right)^2\right].$$

To simplify notations, in this equation and those that follow in this subsection, energies are in units of t_0, and $\hbar = 1$. For a given group-velocity direction φ, $\mathbf{q}$ needs to satisfy the

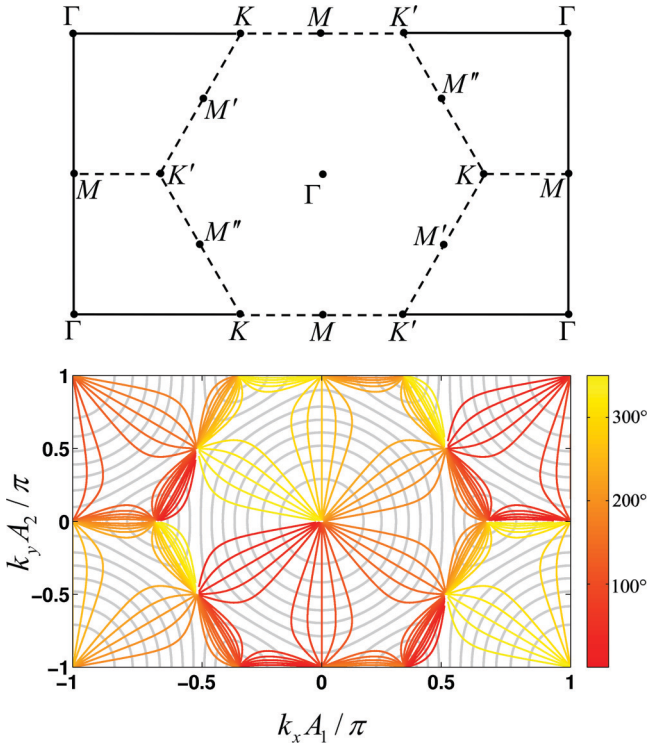

FIG. 5. (Color online) Contour of group velocities of the same direction φ in the Brillouin zone. The contour is denoted by lines fanning out from the origin (Γ point) and other special points labeled in the top figure. Background concentric circles enclosing the origin are energy contour lines.

condition

$$t \equiv \tan\varphi = \frac{\partial E(\mathbf{q})/\partial q_y}{\partial E(\mathbf{q})/\partial q_x}.$$

After a straightforward but lengthy derivation, the dip positions are found to be at

$$E = \pm\alpha\left(q_y^0 + \Delta q_y\right) + \omega, \tag{21}$$

where for the plus branch, $q_y^0 = \omega t/(\alpha\gamma)$ and

$$\Delta q_y \simeq -\frac{4\mu}{3}\frac{\omega^2 t}{\alpha\gamma^2}\frac{1}{1 - \gamma t + \mu\,\omega[1/\gamma + 5t/3]}. \tag{22}$$

For the minus branch, $q_y^0 = \omega\gamma t/\alpha$ and

$$\Delta q_y \simeq -\frac{\mu}{6}\frac{\omega^2 t}{\alpha}\frac{9\gamma^2 + 2\gamma t - 1}{1 + t/\gamma + \mu\,\omega[\gamma - 5t/3]}. \tag{23}$$

Here $\gamma = \sqrt{1+t^2} - t$. The valley dependence of the dip-structure positions is carried by μ's in Δq_y. Excellent numerical agreement of these expressions to the dip-structure positions in Fig. 3 and Fig. 7 lends an unequivocal confirmation of the physical origin of the dip structures, namely resonant sideband processes via a relevant band edge. This making of the resonant condition is a generic feature of the coherent inelastic resonance in transmission.[58,59]

B. Nontypical Fabry-Pérot resonance

In this subsection, we show that the dip amplitude of the $T^{(\mu)}$ dip structures can be tuned by L, the length of the

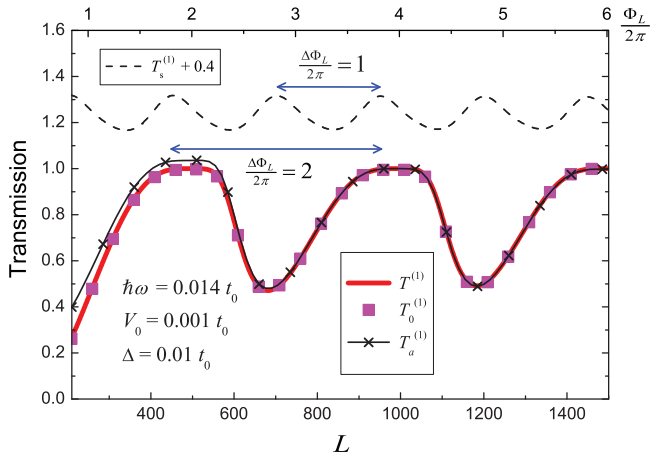

FIG. 6. (Color online) L dependence of the current transmission dip-structure amplitude for a time-dependent-potential region in a gapped graphene ($\Delta = 0.01t_0$). The dip-structure condition is $E_0 = \Delta + \hbar\omega$. Parameters for the time-modulated potential are $\hbar\omega = 0.014\,t_0$ and $V_0 = 0.001\,t_0$. Normal incidence case is shown. Presented are the full numerical result $T^{(1)}$ (solid curve), results for $T_0^{(1)}$ (solid square), and for $T_a^{(1)}$ (crossed thin line). The L dependence of transmission $T_s^{(1)}$ (dashed curve) through a static potential ($V_s = 0.5\,t_0$) region is plotted, for contrast, with incident energy $E_i = \Delta + \hbar\omega - V_s$. The T_s curve is vertically shifted by 0.4.

time-modulated-potential region. The underlying mechanism, as we find out, is not of a Febry-Pérot-type resonance, but is a nontypical one that is the result of a coherent inelastic resonance instigated by the relevant band edge for the first sideband process.

We show in Fig. 6 that the dip amplitude, depicted by the solid curve, exhibits an oscillatory dependence on L. Normal incidence case is considered here. The $T^{(1)}$ dip structure we focus upon is the $E_0 = \Delta + \hbar\omega$ dip structure in Fig. 4, but for $\hbar\omega = 0.014\,t_0$, $V_0 = 0.001\,t_0$, and $L \leqslant 1500$. Our plot of the $T_0^{(1)}$ dip amplitude (solid square) shows that it dominates the total current transmission $T^{(1)}$.

For the purpose of comparing the L dependence, we also plot in Fig. 6 a $T_s^{(1)}$ (dashed) curve due to a static barrier. The barrier height $V_s = 0.5\,t_0$, barrier width (longitudinal) L, and for incident energy $E_i = \Delta + \hbar\omega - V_s$. This choice of E_i is to give the same $q_0^{(\mu)}$ and $p_0^{(\mu)}$ in our case in the multiple-scattering region. The oscillatory behavior in $T_s^{(1)}$ is of a Febry-Pérot type, characterized by the condition $\Phi_L = 2\pi$, where

$$\Phi_L \equiv \left(p_0^{(1)} - q_0^{(1)}\right) A_1\, L \tag{24}$$

is the phase picked up in a round trip inside the scattering region. Here, the momenta in the barrier region have $|\mathbf{p}_0^{(1)} - K_0\hat{x}| = |\mathbf{q}_0^{(1)} - K_0\hat{x}|$ such that $\Phi_L = 2|\mathbf{p}_0^{(1)} - K_0\hat{x}|\,LA_1$. The two different oscillatory behaviors in Fig. 6 show that the dip-amplitude period doubles that for the static barrier. In other words, the phase picked up in a round trip inside the scattering region for the resonant sideband processes could be $\Phi_L/2$. The dip-amplitude oscillatory behavior in Fig. 6 hence belongs to a nontypical Febry-Pérot resonance. A multiple scattering analysis is shown below to trace out the physical origin of the $\Phi_L/2$.

Following Eq. (19), the transmission coefficient $\mathcal{T}_0^{(1)}$ is expressed in the form

$$\mathcal{T}_0^{(1)} = \sum_{\alpha,\beta} [\mathbf{t}_2']_{0\alpha} \left[\frac{\mathbf{1}}{\mathbf{1} - \mathbf{r}_1\mathbf{r}_2'}\right]_{\alpha\beta} [\mathbf{t}_1']_{\beta 0}, \tag{25}$$

where the matrix elements

$$\begin{aligned}
[\mathbf{r}_1]_{mn} &= \left\langle p_m^{(1)}\middle|\mathbf{r}_1\middle|q_n^{(1)}\right\rangle, \quad [\mathbf{t}_1]_{mn} = \left\langle q_m^{(1)}\middle|\mathbf{t}_1\middle|q_n^{(1)}\right\rangle,\\
[\mathbf{r}_2']_{mn} &= \left\langle q_m^{(1)}\middle|\mathbf{r}_2'\middle|p_n^{(1)}\right\rangle, \quad [\mathbf{t}_2']_{mn} = \left\langle p_m^{(1)}\middle|\mathbf{t}_2'\middle|p_n^{(1)}\right\rangle,\\
[\mathbf{t}_1']_{mn} &= \left\langle p_m^{(1)}\middle|\mathbf{t}_1'\middle|p_n^{(1)}\right\rangle.
\end{aligned}$$

Essentially, the indices α and β in Eq. (25) denote the sideband indices of the intermediate processes, while both the starting and the final sideband are $n = 0$.

To trace out how L enters Eq. (25), all we need to do is to take note of the reflection and transmission matrices, $\mathbf{r}_2'$ and $\mathbf{t}_2'$, respectively, at the interface $M = L$. Expressed in terms of the corresponding matrices $\mathbf{r}_1$ and $\mathbf{t}_1$ at the interface $M = 0$, the matrices are given by

$$\begin{aligned}
[\mathbf{r}_2']_{mn} &= [\mathbf{r}_1]_{mn} e^{-i(q_m^{(1)} - p_n^{(1)})LA_1},\\
[\mathbf{t}_2']_{mn} &= [\mathbf{t}_1]_{mn} e^{-i(p_m^{(1)} - p_n^{(1)})LA_1}.
\end{aligned} \tag{26}$$

At the dip structure, we can simplify things by keeping only the incident and the first sideband channels $n = 0$, and $n = -1$ (or $\bar{1}$), respectively, for our multiple scattering analysis. We note that the reflection and transmission matrices we kept are calculated at a single interface and with many sidebands included. Already, we see that the phases in Eq. (26) are related to $\Phi_L/2$. For instance, for the $(mn) = (0\bar{1})$ case, we have $(p_{\bar{1}}^{(1)} - q_0^{(1)})LA_1$ equals $\Phi_L/2$, because $p_{\bar{1}}^{(1)} - K_0\hat{x} = 0$. The reduced-dimension matrices are given by

$$\begin{aligned}
\tilde{\mathbf{r}}_2' &= \begin{pmatrix} [\mathbf{r}_2']_{00} & [\mathbf{r}_2']_{0\bar{1}} \\ [\mathbf{r}_2']_{\bar{1}0} & [\mathbf{r}_2']_{\bar{1}\bar{1}} \end{pmatrix}\\
&= \begin{pmatrix} [\mathbf{r}_1]_{00} e^{i\Phi_L} & [\mathbf{r}_1]_{0\bar{1}} e^{i\Phi_L/2} \\ [\mathbf{r}_1]_{\bar{1}0} e^{i\Phi_L/2} & [\mathbf{r}_1]_{\bar{1}\bar{1}} \end{pmatrix},\\
\tilde{\mathbf{t}}_2' &= \begin{pmatrix} [\mathbf{t}_2']_{00} & [\mathbf{t}_2']_{0\bar{1}} \\ [\mathbf{t}_2']_{\bar{1}0} & [\mathbf{t}_2']_{\bar{1}\bar{1}} \end{pmatrix}\\
&= \begin{pmatrix} [\mathbf{t}_1]_{00} & [\mathbf{t}_1]_{0\bar{1}} e^{-i\Phi_L/2} \\ [\mathbf{t}_1]_{\bar{1}0} e^{i\Phi_L/2} & [\mathbf{t}_1]_{\bar{1}\bar{1}} \end{pmatrix}.
\end{aligned} \tag{27}$$

Correspondingly, the transmission coefficient in Eq. (25) is replaced by

$$\tilde{\mathcal{T}}_0^{(1)} = \sum_{\alpha,\beta} [\tilde{\mathbf{t}}_2']_{0\alpha} \left[\frac{\mathbf{1}}{\mathbf{1} - \tilde{\mathbf{r}}_1\tilde{\mathbf{r}}_2'}\right]_{\alpha\beta} [\tilde{\mathbf{t}}_1']_{\beta 0},$$

where

$$\left[\frac{\mathbf{1}}{\mathbf{1} - \tilde{\mathbf{r}}_1\tilde{\mathbf{r}}_2'}\right]_{\alpha\beta} = \frac{\delta_{\alpha\beta} + (\mathbf{1} - 2\delta_{\alpha\beta})[\tilde{\mathbf{r}}_1\tilde{\mathbf{r}}_2']_{\alpha\beta}}{\det(\mathbf{1} - [\tilde{\mathbf{r}}_1\tilde{\mathbf{r}}_2'])}. \tag{28}$$

The L dependence of the dip-structure amplitude we get from $T_a^{(1)} \equiv |\tilde{\mathcal{T}}_0^{(1)}|^2$ matches remarkably with the full numerical result, as shown in Fig. 6. It is sufficient to look at $\det(\mathbf{1} - [\tilde{\mathbf{r}}_1\tilde{\mathbf{r}}_2'])$ for the L dependence. With

$$\det(\mathbf{1} - [\tilde{\mathbf{r}}_1\tilde{\mathbf{r}}_2']) = h_0 + h_1 e^{i\Phi_L/2} + h_2 e^{i\Phi_L}, \tag{29}$$

where

$$h_0 = 1 - [\mathbf{r}_1]^2_{\bar{1}\bar{1}},$$
$$h_1 = -2[\mathbf{r}_1]_{\bar{1}0}[\mathbf{r}_1]_{0\bar{1}},$$
$$h_2 = -h_0[\mathbf{r}_1]^2_{00}, -2[\mathbf{r}_1]_{0\bar{1}}[\mathbf{r}_1]_{\bar{1}\bar{1}}[\mathbf{r}_1]_{\bar{1}0}[\mathbf{r}_1]_{00} + [\mathbf{r}_1]^2_{\bar{1}0}[\mathbf{r}_1]^2_{0\bar{1}}$$

are functions independent on L, we see that the L period in $\det(\mathbf{1} - [\tilde{\mathbf{r}}_1\tilde{\mathbf{r}}'_2])$ is determined by the phase factor $e^{i\Phi_L/2}$, leading to the condition $\Phi_L = 4\pi$. This phase factor, according to Eq. (27), is originated from the resonant first-sideband process to the relevant band edge. In short, the inelastic nature of the resonance allows the electron to accumulate a phase in its round trip around the scattering region from two wave vectors of different magnitudes. This is in contrast to a Febry-Pérot resonance, where the two wave vectors are of the same magnitude. The nontypical Febry-Pérot feature in the dip-structure amplitudes is thus another manifestation of the generic feature of the coherent inelastic resonances.

IV. CONCLUSIONS

In this paper, we have demonstrated the valley-dependent resonant inelastic transmission through a time-modulated region in graphene. We have shown explicitly that this results from a remarkable interplay between the trigonal-warping effect and the generic nature of the coherent inelastic resonance in transmission. The coherent inelastic resonance imposes the condition for the occurrence of the transmission dip structures to be the sideband process to a relevant band edge. The trigonal-warping effect provides a valley-dependent relevant band edge for the dip structures. This resonant condition does not involve L. It is evident in Eq. (21), Eq. (22), and Eq. (23), and in the excellent agreement of these expressions to the dip-structure positions in Fig. 3 and Fig. 7, where L's are different.

In contrast, trigonal-warping exerts its effect differently in the case of tunneling through time-independent potential barriers in graphene,[35] as far as the resonant condition is concerned. The resonance is established by the Febry-Pérot processes within the barriers, while the trigonal warping provides valley-dependent wave vectors for the phase accumulation in the multiple scattering processes. Consequently L, or the longitudinal configuration of the potential barriers, will affect the resonant condition.[35] On the other hand, in our case, that the resonant condition is free from L is a noteworthy feature. It allows a simpler connection between the dip positions and the frequency ω. This feature might be worth future exploration on possible application to frequency detection. We stress, in addition, that the multiple scattering in our case sets up the nontypical Febry-Pérot feature in our dip-structure amplitudes, allows the L tuning of the dip amplitudes, but does not determine the dip position.

Collimation, the fixing of the group velocity direction φ of the incident flow, is important for the observation of the findings in this work. It has been realized in two-dimensional electron systems, by the alignment of two point contacts in series.[60,61] This work points out the importance to valleytronics of realizing such collimation in graphene. The two aligned point contacts would need to be etched out of graphene, with both the transverse width of the point contacts and the spatial separation between point contacts much greater than the

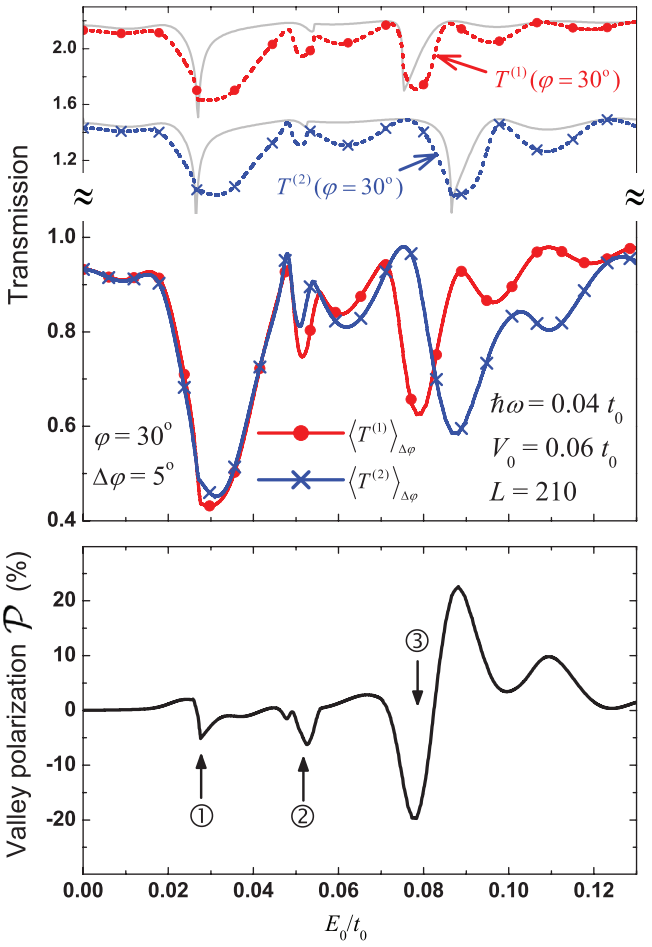

FIG. 7. (Color online) Averaged current transmission $\langle T^{(\mu)}\rangle_{\Delta\varphi}$ and valley polarization $\mathcal{P}$ versus incident energy E_0. Top figure shows $\langle T^{(\mu)}\rangle_{\Delta\varphi}$ (solid curves), $T^{(\mu)}$ (dotted curves), and $T^{(\mu)}$ (gray curves) of 0.53 V_0. Parameters $\hbar\omega = 0.04t_0$, $V_0 = 0.06t_0$, $L = 210$, $\varphi = 30^\circ$, and $\Delta\varphi = 5^\circ$. In the bottom figure, the valley polarization $\mathcal{P}$ (solid curve) has dip structures (arrows 1 and 2) due to $-E^*_B + \hbar\omega$ and $-E^*_B + 2\hbar\omega$ resonant conditions, respectively. The dip-and-peak structure (arrow 3) is due to $E^*_B + \hbar\omega$ resonant condition.

electron wavelength.[60,61] The orientation of the point contact on the graphene lattice would have fixed the φ for the incident electron flow.

Averaging our results over φ on a range $\varphi \pm \Delta\varphi/2$, we show in Fig. 7 (bottom figure) that the valley polarization $\mathcal{P}$ in the transmission remains significant. Here, $\varphi = 30^\circ$ and $\Delta\varphi = 5^\circ$. Dip structures on the curve, indicated by arrows 1 and 2, correspond to resonant conditions $-E^*_B + n\hbar\omega$, while the dip-and-peak structure, indicated by arrow 3, corresponds to the resonant condition $E^*_B + \hbar\omega$. The valley polarization is defined as

$$\mathcal{P} = \frac{\langle T^{(1)}\rangle_{\Delta\varphi} - \langle T^{(2)}\rangle_{\Delta\varphi}}{\langle T^{(1)}\rangle_{\Delta\varphi} + \langle T^{(2)}\rangle_{\Delta\varphi}},$$

where $\langle T^{(\mu)}\rangle_{\Delta\varphi}$ is the averaged transmission. For reference, we plot, in Fig. 7 (upper figure), the averaged transmission $\langle T^{(\mu)}\rangle_{\Delta\varphi}$ (solid curves) and the transmission $T^{(\mu)}$ (dotted curves) at $\varphi = 30^\circ$. The transmission $T^{(\mu)}$ (gray curves) for a smaller V_0 is added to better indicate the dip-structure

locations. That the $2\hbar\omega$ sideband process is more evident in Fig. 7 than in Fig. 3 is because of a larger $V_0/\hbar\omega$ [see Eq. (12)]. This is essentially due to a smaller $\hbar\omega = 0.04t_0$, or a frequency of $\omega/2\pi = 25.7$ THz. For an even smaller $\hbar\omega = 0.02t_0$ (or frequency ~ 12 THz), and $V_0 = 0.03t_0$, our finding (not shown) is that the dip-peak structure in $\mathcal{P}$ ranges between $\pm 10\%$ for the $E_B^* + \hbar\omega$ resonance. Thus our results are within reach of the experimental capability,[62] for the case of graphene. Finally, we point out that the valley polarization $\mathcal{P}$ in Fig. 7 does not depend on the magnitude of t_0. Thus in artificial honeycomb lattices,[63] when t_0 could be scaled down, the frequency needed for the observation of the phenomenon in this work would have been scaled down accordingly, to well within the THz range. Thus our finding should also be relevant to the recent work on artificial honeycomb lattices.[63]

In conclusion, we have studied the transmission of electrons through a time-modulated-potential region in graphene. Coherent sideband processes are found to be at work in the low energy regime even for the case of a pristine graphene, when the full electron dispersion is gapless. The relevant energy band and its band edge in the case of non-normal incident provide a favorable condition for the coherent sideband processes, and to the formation of dip structures in the transmission. A collimated incident beam is shown to exhibit valley-dependent dip-structure characteristics, due to the trigonal warping effects. Our results should be of interest to valleytronics in graphene, and possible implications to the THz studies and artificial honeycomb lattices are also discussed.

ACKNOWLEDGMENTS

This work was supported by Taiwan NSC (Contract No. 101-2112-M-009-014), NCTS Taiwan, and a MOE-ATU grant.

*li923358@cc.nctu.edu.tw
†cschu@cc.nctu.edu.tw

[1] K. S. Novoselov, A. K. Geim, S. V. Morozov, D. Jiang, Y. Zhang, S. V. Dubonos, I. V. Grigorieva, and A. A. Firsov, Science **306**, 666 (2004).
[2] K. S. Novoselov, D. Jiang, F. Schedin, T. J. Booth, V. V. Khotkevich, S. V. Morozov, and A. K. Geim, Proc. Natl. Acad. Sci. USA **102**, 10451 (2005).
[3] A. K. Geim and K. S. Novoselov, Nat. Mater. **6**, 183 (2007).
[4] C. W. J. Beenakker, Rev. Mod. Phys. **80**, 1337 (2008).
[5] A. H. Castro Neto, F. Guinea, N. M. R. Peres, K. S. Novoselov, and A. K. Geim, Rev. Mod. Phys. **81**, 109 (2009).
[6] N. M. R. Peres, Rev. Mod. Phys. **82**, 2673 (2010).
[7] D. Abergel, V. Apalkov, J. Berashevich, K. Ziegler, and T. Charkraborty, Adv. Phys. **59**, 261 (2010).
[8] S. DasSarma, S. Adam, E. H. Hwang, and E. Ross, Rev. Mod. Phys. **83**, 407 (2011).
[9] V. N. Kotov, B. Uchoa, V. M. Pereira, F. Guinea, and A. H. C. Castro Neto, Rev. Mod. Phys. **84**, 1067 (2012).
[10] P. Avouris, Z. Chen, and V. Perebeinos, Nat. Nanotech. **2**, 605 (2007).
[11] Y. W. Son, M. L. Cohen, and S. G. Louie, Nature (London) **444**, 347 (2006).
[12] F. Miao, S. Wijeratne, Y. Zhang, U. C. Coskun, W. Bao, and C. N. Lau, Science **317**, 1530 (2007).
[13] L. A. Ponomarenko, F. Schedin, M. I. Katsnelson, R. Yang, E. W. Hill, K. S. Novoselov, and A. K. Geim, Science **320**, 356 (2008).
[14] X. Wang, Y. Ouyang, X. Li, H. Wang, J. Guo, and H. Dai, Phys. Rev. Lett. **100**, 206803 (2008).
[15] F. N. Xia, T. Mueller, Y. M. Lin, A. Valdes-Garcia, and P. Avouris, Nat. Nanotech. **4**, 839 (2009).
[16] F. Schwierz, Nat. Nanotech. **5**, 487 (2010).
[17] P. Avouris and F. N. Xia, MRS Bulletin **37**, 1225 (2012).
[18] M. I. Katsnelson, K. S. Novoselov, and A. K. Geim, Nat. Phys. **2**, 620 (2006).
[19] K. S. Novoselov, A. K. Geim, S. V. Morozov, D. Jiang, M. I. Katsnelson, I. V. Grigorieva, S. V. Dubonos, and A. A. Firsov, Nature (London) **438**, 197 (2005).
[20] Y. Zhang, J. W. Tan, H. L. Stormer, and P. Kim, Nature (London) **438**, 201 (2005).
[21] H. Suzuura and T. Ando, Phys. Rev. Lett. **89**, 266603 (2002).
[22] E. McCann, K. Kechedzhi, V. I. Fal'ko, H. Suzuura, T. Ando, and B. L. Altshuler, Phys. Rev. Lett. **97**, 146805 (2006).
[23] A. F. Morpurgo and F. Guinea, Phys. Rev. Lett. **97**, 196804 (2006).
[24] V. V. Chelanov, V. Fal'kov, and B. L. Altshuler, Science **315**, 1252 (2007).
[25] S. Gómez, P. Burset, W. J. Herrera, and A. L. Yeyati, Phys. Rev. B **85**, 115411 (2012).
[26] C. H. Park, Y. W. Son, L. Yang, M. L. Cohen, and S. G. Louie, Nano Lett. **8**, 2920 (2008).
[27] M. Fujita, K. Wakabayashi, K. Nakada, and K. Kusakabe, J. Phys. Soc. Jpn. **65**, 1920 (1996).
[28] S. Ryu and Y. Hatsugai, Phys. Rev. Lett. **89**, 077002 (2002).
[29] C. L. Kane and E. J. Mele, Phys. Rev. Lett. **95**, 226801 (2005).
[30] W. Yao, S. A. Yang, and Q. Niu, Phys. Rev. Lett. **102**, 096801 (2009).
[31] Z. H. Qiao, S. Y. A. Yang, B. Wang, Y. G. Yao, and Q. Niu, Phys. Rev. B **84**, 035431 (2011).
[32] C. H. Chiu and C. S. Chu, Phys. Rev. B **85**, 155444 (2012).
[33] A. Rycerz, J. Tworzydlo, and C. W. J. Beenakker, Nat. Phys. **3**, 172 (2007).
[34] J. L. Garcia-Pomar, A. Cortijo, and M. Nieto-Vesperinas, Phys. Rev. Lett. **100**, 236801 (2008).
[35] J. M. Pereira, F. M. Peeters, R. N. Costa Filho, and G. A. Farias, J. Phys.: Condens. Matter **21**, 045301 (2009).
[36] A. Chaves, L. Covaci, K. Y. Rakhimov, G. A. Farias, and F. M. Peeters, Phys. Rev. B **82**, 205430 (2010).
[37] D. Gunlycke and C. T. White, Phys. Rev. Lett. **106**, 136806 (2011).
[38] A. R. Akhmerov and C. W. J. Beenakker, Phys. Rev. Lett. **98**, 157003 (2007).
[39] D. Xiao, W. Yao, and Q. Niu, Phys. Rev. Lett. **99**, 236809 (2007).
[40] Z. H. Wu, F. Zhai, F. M. Peeters, H. Q. Xu, and K. Chang, Phys. Rev. Lett. **106**, 176802 (2011).
[41] Y. Jiang, T. Low, K. Chang, M. I. Katsnelson, and F. Guinea, Phys. Rev. Lett. **110**, 046601 (2013).
[42] P. Recher, B. Trauzettel, A. Rycerz, Ya. M. Blanter, C. W. J. Beenakker, and A. F. Morpurgo, Phys. Rev. B **76**, 235404 (2007).

[43]G. Y. Wu, N. Y. Lue, and L. Chang, Phys. Rev. B **84**, 195463 (2011).
[44]B. Trauzettel, Ya. M. Blanter, and A. F. Morpurgo, Phys. Rev. B **75**, 035305 (2007).
[45]M. A. Zeb, K. Sabeeh, and M. Tahir, Phys. Rev. B **78**, 165420 (2008).
[46]C. G. Rocha, Luis E. F. Foa Torres, and G. Cuniberti, Phys. Rev. B **81**, 115435 (2010).
[47]R. P. Tiwari and M. Blaauboer, Appl. Phys. Lett. **97**, 243112 (2010).
[48]P. San-Jose, E. Prada, S. Kohler, and H. Schomerus, Phys. Rev. B **84**, 155408 (2011).
[49]W. T. Lu, S. J. Wang, W. Li, Y. L. Wang, and C. Z. Ye, J. Appl. Phys. **111**, 103717 (2012).
[50]S. E. Savel'ev, W. Hausler, and P. Hanggi, Phys. Rev. Lett. **109**, 226602 (2012).
[51]S. V. Syzranov, M. V. Fistul, and K. B. Efetov, Phys. Rev. B **78**, 045407 (2008).
[52]N. H. Lindner, G. Refael, and V. Galitski, Nat. Phys. **7**, 490 (2011).
[53]Y. Zhou and M. W. Wu, Phys. Rev. B **83**, 245436 (2011).
[54]Z. G. Gu, H. A. Fertig, D. P. Arovas, and A. Auerbach, Phys. Rev. Lett. **107**, 216601 (2011).
[55]T. Kitagawa, T. Oka, A. Brataas, L. Fu, and E. Demler, Phys. Rev. B **84**, 235108 (2011).
[56]C. Sinha and R. Biswas, Appl. Phys. Lett. **100**, 183107 (2012).
[57]P. San-Jose, E. Prada, H. Schomerus, and S. Kohler, Appl. Phys. Lett. **101**, 153506 (2012).
[58]P. F. Bagwell and R. K. Lake, Phys. Rev. B **46**, 15329 (1992).
[59]C. S. Tang and C. S. Chu, Phys. Rev. B **53**, 4838 (1996).
[60]C. W. J. Beenakker and H. van Houten, Phys. Rev. B **39**, 10445(R) (1989).
[61]L. W. Molenkamp, A. A. M. Staring, C. W. J. Beenakker, R. Eppenga, C. E. Timmering, J. G. Williamson, C. J. P. M. Harmans, and C. T. Foxon, Phys. Rev. B **41**, 1274(R) (1990).
[62]L. Ju, B. S. Geng, J. Horng, C. Girit, M. Martin, Z. Hao, H. A. Bechtel, X. G. Liang, A. Zettl, Y. R. Shen, and F. Wang, Nat. Nanotech. **6**, 630 (2011).
[63]M. Polini, F. Guinea, M. Lewenstein, H. C. Manoharan, and V. Pellegrini, Nat. Nanotech. **8**, 625 (2013).